Electron-phonon interactions and two-phonon modes associated with charge density wave in single crystalline 1T-VSe$_2$

Juhi Pandey and Ajay Soni[*]

School of Basic Sciences, Indian Institute of Technology Mandi, Mandi 175075, Himachal Pradesh, India

The charge density wave (CDW) is a unique phenomenon mostly realized in two-dimensional (2D) metallic layered transition metal dichalcogenides. We report on the observation of commensurate CDW (C-CDW) and incommensurate (I-CDW) transition in single crystal 1T-VSe$_2$ using the spectroscopy technique in the temperature range of 50–120 K. The room temperature Raman spectra showed a sharp A_{1g} mode $\sim$206 cm^{-1} along with two additional modes associated to $E_g \sim 257$ cm^{-1} symmetry and two-phonon (2_{ph}) ~ 332 cm^{-1} interactions. The onset temperature of I-CDW and C-CDW is estimated from resistance measurements supported by magnetic measurements. Remarkably, at the onset of I-CDW $\sim$ 115 K, a significant enhancement in the intensity of the weak E_g mode is observed along with emergence of a doubly degenerate $E_g(2)$ mode $\sim$144 cm^{-1}, while below 70 K, the emergence of the A_{1g} mode $\sim$170 cm^{-1} signifies the onset of C-CDW. The observation of a sudden rise in the intensity of the E_g mode $\sim$257 cm^{-1} mode, below I-CDW, showed the involvement of electron-phonon coupling in 1T-VSe$_2$.

I. INTRODUCTION

The charge density wave (CDW) is a low-temperature ordered phase that arises from periodic modulation of conduction electron densities accompanied by periodic distortion of the atomic lattice [1–3]. The commonly accepted argument for the origin of the CDW, in many low-dimensional systems, is based on the Peierls picture described for purely one-dimensional metallic systems, where electronic instabilities result in Fermi-surface nesting. Here, the CDW is said to be driven by Fermi-surface nesting since the contour of a Fermi surface coincides with ordering vector Q [4]. However, there are several recent reports suggesting that nesting alone is insufficient to explain the CDW. In many cases, especially for two dimensions (2D) and higher dimensions, the Fermi surface does not nest at the ordering vector Q [5,6]. For instance, in the cases of 2H-NbSe$_2$, CeTe$_3$, and ErTe$_3$, strong electron-phonon coupling plays a more important role for determining Q than Fermi-surface nesting [7,8]. Based on the periodicity of Q, th eCDW has been classified as commensurate CDW (C-CDW), nearly commensurate (N-CDW), and incommensurate CDW (I-CDW) with a high-symmetry phase. In the C-CDW phase, the Q is an integral multiple of the reciprocal lattice vector of the undistorted phase, whereas in the I-CDW phase it is not [9].

Layered transition metal dichalcogenides (TMDCs) provide a rich platform for research with their wide range of physical properties varying from metallic, semiconducting, superconducting, and magnetism to having exotic optical properties [10–12]. Most 2D materials exist in two stable crystal structures such as 2H (trigonal prismatic) and 1T (octahedron), where the physical properties depend on the symmetry of the phases [13]. Among the several versatile properties, the CDW is a novel phenomenon realized in 1T and 2H polytypes of many metallic layered TMDCs, such as NbSe$_2$, TaSe$_2$, TaS$_2$, VTe$_2$, and VSe$_2$ [14–20]. Thus, these materials have received much scientific and technological attention for many-body interactions and potential applications in memory devices, transistors, logic-gate electronics, and oscillators [14–20]. The origin of the CDW in TMDCs has not achieved any general scientific consensus and has remained a topic of investigation so far [5,21–24]. For 2D systems such as 2H-NbSe$_2$, 2H-TaS$_2$, and 2H-TaSe$_2$ [25,26], electron-phonon coupling plays a major role in CDW compared to Fermi-surface nesting. 1T-VSe$_2$ is isostructural with 1T-TaS$_2$ and 1T-TaSe$_2$, [9,24,27] and is expected to show similar anomaly in resistivity measurement at the CDW, but unlike these isostructural compounds showing a sharp anomaly in resistivity at CDW transitions [28,29], VSe$_2$ shows a gradual upturn similar to 2H-NbSe$_2$, 2H-TaS$_2$, and 2H-TaSe$_2$ [30–32].

VSe$_2$ is a compound that has been intensively studied for its interesting electronic band structure and CDW. The bulk VSe$_2$ crystallizes in the 1T polytype, where the V atoms are covalently bonded with the octahedra of Se atoms to form a single layer of VSe$_2$ and these layers are further stacked through van der Waals interactions [33]. 1T-VSe$_2$ shows I-CDW transition $\sim$110 K and C-CDW transition $\sim$80 K which have been studied using the x-ray diffraction technique, [9] inelastic x-ray scattering technique, angle-resolved

*ajay@iitmandi.ac.in

photoemission spectroscopy [34], and transport measurement [35]. However, because of the high reflectivity of this compound, the obtained optical signals are extremely poor; thus several properties such as vibrational properties, and electron-phonon coupling are not well understood. Thus, in this paper, we have studied the electron-phonon coupling driven CDW transitions in bulk single crystal 1T-VSe$_2$, using temperature-dependent resistivity, magnetic susceptibility, and Raman spectroscopy measurements. The coupling between electron and phonon, at low temperatures, is demonstrated from resistivity as well as magnetic measurements, while spectroscopy is used as a tool to access the CDW in VSe$_2$.

II. EXPERIMENTAL SECTION

A single crystal of VSe$_2$ was grown by reacting a stoichiometric amount of vanadium chips and selenium pellets (both from Sigma-Aldrich, 99.9%) using the chemical vapor transport method with iodine as the transport agent ($\sim$2 kg/m^3). The reactants were vacuum sealed in a quartz ampoule and placed in a two-zone furnace, which was heated slowly ($\sim$20 h) to reach the growth temperatures of 1093 K (hot zone) and 923 K (cold zone). The samples were kept in the gradient temperature for $\sim$72 h followed by slow cooling to room temperature over $\sim$20 h. Thus, large shiny crystals of VSe$_2$ were obtained at the cold end of the tube. X-ray diffraction (XRD) of the prepared crystals was obtained using a rotating anode Rigaku SmartLab diffractometer in Bragg-Brentano geometry with Cu $K\alpha$ radiation ($\lambda = 1.5406$ Å) . To determine the crystal structure and phase purity, Rietveld refinement of the XRD patterns was done using FULLPROF SUITE software [36].

Four-probe electrical resistance (R) and magnetic susceptibility (χ) measurements were performed from 2 to 300 K using a Quantum Design physical properties measurement system and magnetic properties measurement system, respectively. Micro-Raman measurements were done using a Horiba Jobin-Yvon LabRAM HR evolution Raman spectrometer in backscattering geometry with solid state laser excitation ($\sim$532 nm), 1800 grooves/mm grating, and a Peltier cooled charge-doupled device (CCD) detector. Polarized Raman measurements were performed using two half-wave plates as polarizer and analyzer. Temperature-dependent micro-Raman measurement was performed by using a Montana cryostation in the temperature range of 3–300 K. All the Raman measurements are performed on the (001) plane of 1T-VSe$_2$ single crystal. Field emission scanning electron microscopy (FESEM) images and elemental mapping using energy dispersive spectroscopy (EDS) were recorded through JFEI Nova Nano SEM-450 (see Supplemental Material [37]).

III. RESULTS AND DISCUSSION

The XRD pattern and Rietveld refinement of the VSe$_2$ is shown in Fig. 1(a). The estimated lattice parameters are $a = 3.361$ Å and $c = 6.101$ Å, with a unit cell volume $= 59.726$ Å^3. The difference curve ($Y_{obs} - Y_{calc}$) clearly shows the grown VSe$_2$ crystals are of high-quality single phase while the single crystalline nature is confirmed by observation of peaks only along the c
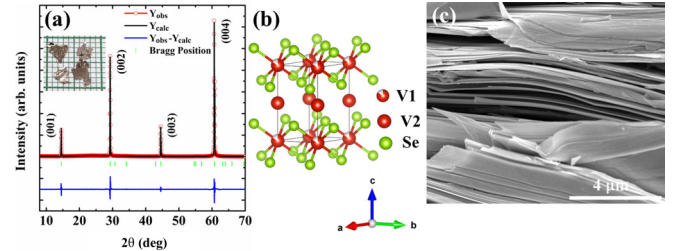

FIG. 1. (a) XRD pattern of single crystal of 1T-VSe$_2$; inset shows the optical image of the grown crystals. (b) Schematic of trigonal crystal structure of $P\bar{3}m1$ space group. (c) FESEM imaging of the layered nature of the crystal.

axis. The inset shows the optical image of the grown crystals with large dimensions ($\sim$5 mm × 5 mm). In general, the VSe$_2$ has trigonal crystal structure with a $P\bar{3}m1$ space group [Fig. 1(b)]; however, there is a mild possibility of self-intercalation of V atoms between the van der Waals gap of VSe$_2$, thus occupying two different sites, V1 (0, 0, 0) and V2 (0, 0, 0.5) [38]. Such self-intercalation is commonly observed due to synthesis at high temperature [39]. Nevertheless, the extent of self-intercalation can be minimized by synthesizing the compound at a lower temperature, $\sim$923 K. The layered nature of the VSe$_2$ crystal is observed through FESEM imaging shown in Fig. 1(c). The stoichiometry of the prepared sample has been estimated using elemental mapping (see Supplemental Material, Table S1 [37]).

The temperature-dependent electrical resistance (R) shows metallic behavior throughout the T range with an onset of the hump below 110 K [Fig. 2(a)]. In general, the close association of structural changes and modifications of the charge density are represented by a hump in $R(T)$, which is a signature of CDW transition in most of the materials. The observations are in line with several layered TMDCs such as 1T-TaS$_2$, 1T-TaSe$_2$, and 2H-TaSe$_2$ [28]. Additionally, the quality of the crystal plays an important role for the onset of CDW transition, and the residual resistance ratio, defined as RRR = $R_{300K}/R_{6.2K}$, is one of the parameters to estimate. Here, the RRR is about 8, which is in good agreement with previous reports and confirms the high quality of the synthesized VSe$_2$ single crystal [35]. We have assessed the temperature range of the CDW transition from temperature derivative of resistivity, dR/dT, where two points of inflection at $T \sim$102 K and $\sim$50 K have been observed. In support to our observations, the temperature-dependent x-ray diffractions studies by Tsutsumi [9] described the periodic lattice distortion wave vector in the reciprocal lattice as $(0.250 \pm 0.003)a^* + (0.314 \pm 0.003)c^*$ in the I-CDW state below 110 K and $(0.250 \pm 0.003)a^* + (0.307 \pm 0.003)c^*$ in the C-CDW state below 85 K. Here, the a^* component is independent of temperature; however, the c^* component shows deviation with temperature suggesting that the origin of incommensurability is along the c axis. Thus, the observed inflections in dR/dT are associated to I-CDW $\sim$ 102 K and C-CDW $\sim$ 50 K.

The inset in Fig. 2(a) shows a low-temperature region below 10 K, where R decreases with temperature and exhibits a minimum at $\sim$6.2 K and then increases up to 2 K. This low-temperature upturn in $R(T)$ can originate from various reasons
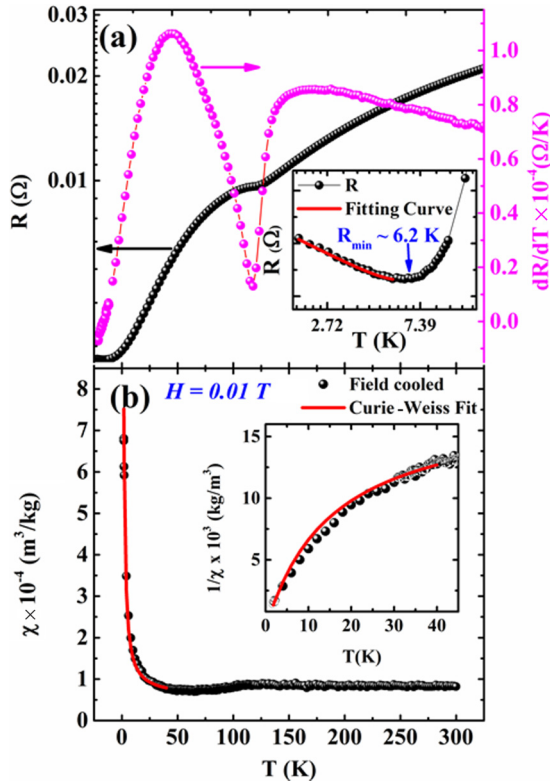
FIG. 2. (a) Resistance (R) and first derivative of resistance (dR/dT) of 1T-VSe$_2$; inset shows upturn in R below 6.2 K due to Kondo interactions. (b) Variation of magnetic susceptibility (χ) with temperature showing downturn at the onset of CDW. The inset figure shows the variation of $1/\chi$ with temperature fitted with modified Curie-Weiss law.

such as weak localization, electron-electron interactions, and the Kondo effect [40,41]. Recently, Barua *et al.* [42] observed a similar upturn in resistivity (ρ) of 1T-VSe$_2$ appearing due to V ions intercalated between the van der Waals gap, which contributed to magnetic susceptibility and acted as localized magnetic scatterers to the conduction electrons. Here, in the case of VSe$_2$, the intercalated V^{4+} ions with an unpaired electron in the d orbital can provide magnetic moments which can drive the electron transport at low temperatures [39,43,44]. This kind of localized magnetic impurity can result in scattering of conduction electrons through s-d exchange interactions and the observed upturn in R(orρ) through such interactions is described as the Kondo effect [42]. We have fitted the low-temperature ρ with $\rho = \rho_0 + \alpha T^2 + c_m \ln(\frac{T_K}{T}) + bT^5$, where ρ_0 is the residual resistivity, αT^2 shows the contribution from the Fermi liquid properties, the term bT^5 is from the lattice vibrations, and $c_m(\ln \frac{T_K}{T})$ represents the contribution from the Kondo effect. Below 6.2 K the logarithmic Kondo term is dominating over other negligible parameters except ρ_0. Thus fitting of the upturn of R below 10 K is suggesting the existence of Kondo-like behavior in VSe$_2$.

To confirm the presence of magnetic moments in 1T-VSe$_2$ because of the intercalated V^{4+} and its effect on the CDW, the temperature-dependent magnetic susceptibility (χ) has been performed and the data are shown in Fig. 2(b). The χ shows a downturn at the onset of the CDW in R measurement. The in-
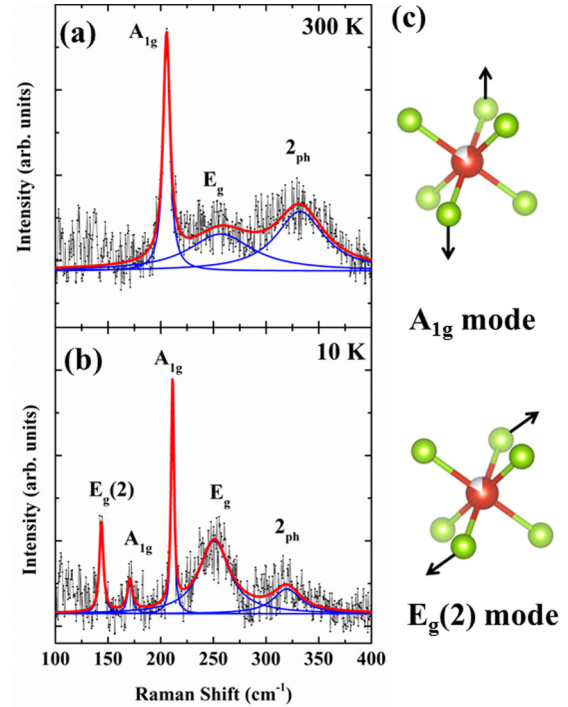

FIG. 3. Raman spectra of 1T-VSe$_2$ at (a) 300 K and (b) 10 K; (c) schematic of main type of lattice vibrations observed in Raman spectra.

set in Fig. 2(b) shows the $1/\chi$ from 1.8 to 40 K (field $\sim$0.01 T) fitted with a modified Curie-Weiss law $\chi(T) = \frac{C}{T-\theta} + \chi_0$, where χ_0 is the temperature-independent intrinsic contribution to susceptibility from the V bands, C is a Curie constant, and θ is a paramagnetic Curie temperature. The parameters obtained from $1/\chi$ fitting using the modified Curie-Weiss law are $\chi_0 = 0.00005$ m^3/kg, $C = 0.0009$ m^3/kg K, and $\theta = 0.5$ K . Thus, the intercalated V is contributing to the feeble magnetism in the sample (shown in Fig. S1, in the Supplemental Material [37]). After confirming the quality of the sample and observation of the signature CDW from low-temperature measurements, we have performed the Raman spectroscopy to understand the phenomena in detail [24].

At high temperatures above the CDW transition, the formula unit of VSe$_2$ has three atoms per unit cell [30,45], and thus has nine zone-center vibrational modes, which can be presented with irreducible representation, $\Gamma = A_{1g} + E_g(2) + 2A_{2u} + 2E_u(2)$. Here only two modes, A_{1g} and the doubly degenerate $E_g(2)$ modes, are Raman active while the other four are IR active modes. [13] Figure 3(a) shows Raman spectra at 300 K having three peaks at $\sim$206, $\sim$257, and $\sim$332 cm^{-1}. For VSe$_2$, Sugai *et al.* [46] reported that the sharp peak at $\sim$206 cm^{-1} is A_{1g} symmetry. Due to the lack of group theoretical analysis of vibrational modes for 1T-VSe$_2$, the origin of the two peaks, $\sim$257 cm^{-1} and $\sim$332 cm^{-1}, could not be understood and thus requires further investigations. To confirm the origin of these modes, we have performed the polarized Raman spectra of the VSe$_2$ crystal (Fig. S2, Supplemental Material [37]), where the laser is incident normal to the ab plane. For parallel polarization (XX) configuration, the incident and the scattered light are polarized along the same

axis, while for perpendicular polarization (*XY*) configuration, they are orthogonal. The sharp A_{1g} mode is observed only in parallel polarization while the mode ~ 257 cm^{-1} is present in both parallel as well as perpendicular polarization measurements [46]. Thus, the mode at ~ 257 cm^{-1} has E_g symmetry. Further, considering the fact that 1T-TiSe$_2$ has similar crystal structure and comparable molecular masses of V and Ti, the origin of these modes can be consigned using the knowledge of the vibrational modes of 1T-TiSe$_2$ [45,47]. Similar to the broad modes, ~ 257 cm^{-1} and 332 cm^{-1}, in 1T-VSe$_2$, weak and broad features are observed at ~ 300 cm^{-1} and 360 cm^{-1} for 1T-TiSe$_2$ which are assigned to A_{1g} symmetry and the two-phonon process [30,47]. Therefore, the broad feature ~ 332 cm^{-1} for 1T-VSe$_2$ can be related with the two-phonon process (2_{ph}) [30].

The low-temperature (10 K) Raman spectra [Fig. 3(b)] has five Raman modes and is quite distinct from the 300 K spectra. The peaks observed, ~ 144 cm^{-1}, ~ 171 cm^{-1}, ~ 211 cm^{-1}, ~ 251 cm^{-1}, and 320 cm^{-1}, are assigned to doubly degenerate the $E_g(2)$, A_{1g}, A_{1g}, E_g, and 2_{ph} modes, respectively [48]. The symmetry assigned for all the modes is based on the symmetry operation on an undisturbed 1T-VSe$_2$ crystal. The schematic of the vibrational modes of A_{1g} ~ 206 cm^{-1} and $E_g(2)$ are shown in Fig. 3(c). Here, the A_{1g} mode represents out-of-plane vibration (along the *c* axis) of Se atoms, while the doubly degenerate $E_g(2)$ mode is associated with the opposite vibration of Se atoms relative to each other along the *a* axis and *b* axis. The $E_g(2)$ mode is expected at 300 K as per the irreducible representation; however, owing to the weak scattering, the mode remains hidden in the noise at 300 K and the intensity of this mode enhances below 120 K. The Raman spectrum shown in Fig. 3 is base line corrected and normalized with the intensity of the A_{1g} mode, ~ 206 cm^{-1}.

To understand the role of the CDW on phonons, we performed a temperature-dependent Raman study from 300 to 10 K, as shown in Fig. 4 (also in Supplemental Material [37], Fig. S3). From 300 to 120 K, three Raman modes, A_{1g}, E_g E_g, and 2_{ph}, have been observed; however, the spectral features are broad and weakly intense for E_g and 2_{ph}. The resemblance in the Raman spectrum from 300 to 120 K confirms the stability of the trigonal structure up to 120 K. However, below 120 K, the intensity of the broad E_g mode starts to rise significantly and becomes comparable with the intensity of the most intense A_{1g} mode. Further, the doubly degenerate $E_g(2)$ mode starts to appear prominently between 100 and 10 K (shown in the red rectangle). Such modulation in the Raman spectra with temperature is related with the onset of the CDW transition below 120 K, as the size of the unit cell increases due to the formation of superlattices [46]. Thus, the vibrational spectra are dramatically modulated by the formation of superlattices, which have been probed by Raman and Fourier transform infrared (FTIR) studies [49].

In the case of incommensurate distortions, the translational symmetry of the lattice is lost and the restriction of first-order Raman scattering to zone-center phonons is relaxed, resulting in several additional modes in the first-order Raman scattering. Interestingly, a very minor peak of A_{1g} ~ 171 cm^{-1} appears at the 40 K spectra and grows further in low-temperature spectra (shown in green rectangle), as reflected in *R* measurement for the onset of the commensurate phase below ~ 50 K.
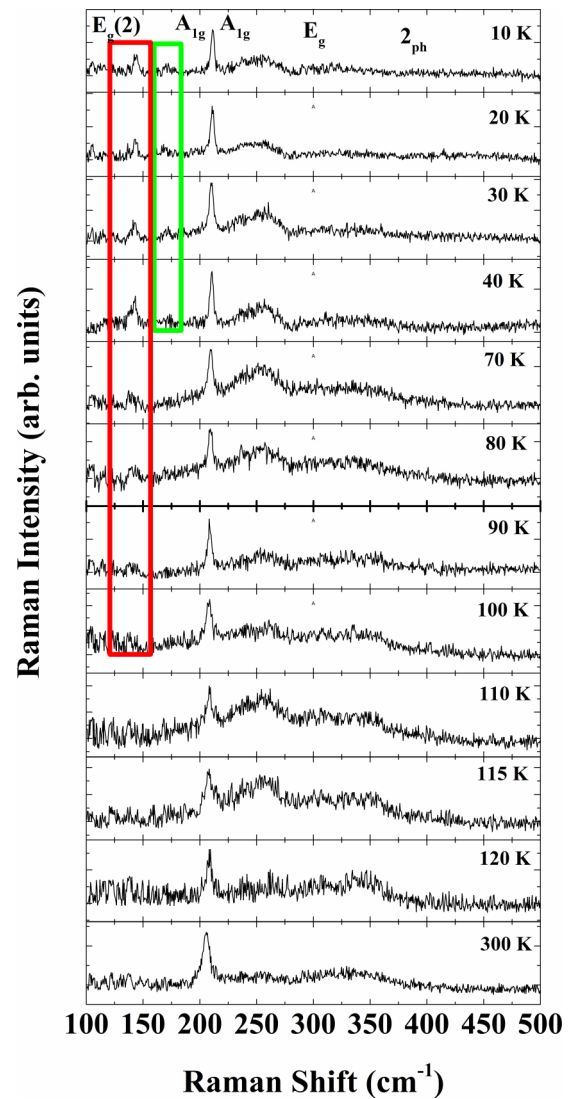

FIG. 4. Temperature dependence of Raman spectra from 300 to 10 K. The enclosed red and green rectangles represent the emergence of $E_g(2)$ at the I-CDW and A_g modes at the C-CDW, respectively.

The behavior can be understood by the formation of a commensurate superlattice where the size of the Brillouin zone reduces, which results in the folding of phonon dispersion curves [24]. This folding can lead to the appearance of new zone-center phonons compared to the undistorted structure. Therefore, the appearance of the out-of-plane A_{1g} mode below 50 K can be associated with the formation of a commensurate superlattice. Further, earlier studies on x-ray investigation of a superlattice at I-CDW and C-CDW transitions demonstrated the significant variation along the c^* axis at the C-CDW transition, whereas the component along the a^* axis remains independent of temperature; therefore the appearance of the out-of-plane A_{1g} mode at ~ 50 K is a signature of C-CDW transition.

To explore the correlation between the CDW transition and phonon energy, the variation of the peak position of the $E_g(2)$ mode, the A_{1g} mode ~ 211 cm^{-1}, and the E_g mode are shown in Fig. 5(a), and the integrated intensity of the E_g mode is shown in Fig. 5(b). The peak position and the integrated
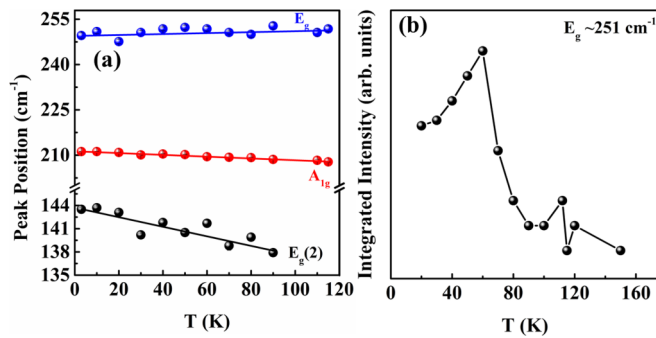
FIG. 5. Temperature dependence of (a) the peak position of the vibrational modes with temperature, and (b) integrated intensity of E_g mode as observed in the normalized Raman spectra.

intensity are determined through the Lorentzian peak fitting of each normalized Raman spectrum. The $E_g(2)$ mode and the A_g mode ~ 211 cm^{-1} show phonon hardening on the lowering of temperature up to 10 K. These modes have been fitted with $\omega(T) = \omega_0 + mT$, where ω_0 is the phonon frequency of the $E_g(2)$ and A_g modes at absolute zero temperature; m is the first-order temperature coefficient of the two modes [50]. The fitted curve is shown as a solid line in Fig. 5(a) and the m values for the $E_g(2)$ and A_g modes obtained by the linear fitting are –0.0617 and -0.0296 cm^{-1}/K, respectively. The stiffening of the phonon mode estimated from m depends upon anharmonic coupling of phonons and thermal expansion of the crystal. In contrast to these two modes showing the usual phonon hardening, the broad E_g mode does not show a significant change in energy with temperature as shown with the solid blue line in Fig. 5(a). However, the integrated intensity of the E_g mode which is active in both the CDW transitions enhances strongly below the I-CDW transition temperature ~ 100 K [Fig. 5(b)]. Further, it is worth noticing that the integrated intensity reaches maxima near C-CDW transition and then starts to decline at further lower

temperature suggesting the coupling of Raman modes with CDW transitions. After the CDW transition, the density of electronic states coupled with phonons decreases at the Fermi surface, which results in the decrease of Raman intensity at further lower temperature. Further, the decrease of the Raman intensity below the C-CDW suggests the deformation of the crystal structure [51]. Thus, the emergence of new Raman modes represents the formation of a superlattice at the onset of the CDW transition and strong coupling of the E_g mode with the CDW, giving evidence of electron-phonon coupling.

IV. CONCLUSION

In summary, the novel phenomenon of the CDW has been investigated in single crystalline 1T-VSe$_2$ using temperature-dependent resistance measurement and Raman spectroscopy. The hump in resistance measurement below 110 K is related to the onset of the I-CDW, while the existence of the C-CDW ~ 50 K is confirmed by dR/dT. The appearance of five Raman active modes at low temperature suggested the reduction in the size of the Brillouin zone due to the formation of superlattices. The onset of the C-CDW transition is marked with the appearance of the A_{1g} mode ~ 177 cm^{-1}. At the onset of the I-CDW, the intensity of the E_g mode, ~ 257 cm^{-1}, enhanced significantly and the $E_g(2)$ mode ~ 114 cm^{-1} becomes prominent. The rise of the integrated intensity of the E_g mode at the onset of the CDW transitions signifies the role of electron-phonon coupling in the CDW transition.

ACKNOWLEDGMENTS

[1] G. Grüner, Rev. Mod. Phys. **60**, 1129 (1988).

[2] P. Leininger, D. Chernyshov, A. Bosak, H. Berger, and D. S. Inosov, Phys. Rev. B **83**, 233101 (2011) .

[3] D. S. Inosov, V. B. Zabolotnyy, D. V. Evtushinsky, A. A. Kordyuk, B. Büchner, R. Follath, H. Berger, and S. V. Borisenko, New J. Phys. **10**, 125027 (2008).

[4] W. Kohn, Phys. Rev. Lett. **2**, 393 (1959).

[5] C. M. Varma and A. L. Simons, Phys. Rev. Lett. **51**, 138 (1983).

[6] M. Lavagnini, M. Baldini, A. Sacchetti, D. DiCastro, B. Delley, R. Monnier, J. H. Chu, N. Ru, I. R. Fisher, P. Postorino, and L. Degiorgi, Phys. Rev. B **78**, 201101(R)(2008).

[7] H.-M. Eiter, M. Lavagninia, R. Hackl, E. A. Nowadnick, A. F. Kemper, T. P. Devereaux, J.-H. Chu, J. G. Analytis, I. R. Fisher, and L. Degiorgi, Proc. Natl. Acad. Sci. USA **110**, 64 (2013).

[8] F. Weber, S. Rosenkranz, J.-P. Castellan, R. Osborn, R. Hott, R. Heid, K.-P. Bohnen, T. Egami, A. H. Said, and D. Reznik, Phys. Rev. Lett. **107**, 107403 (2011).

[9] K. Tsutsumi, Phys. Rev. B **26**, 5756 (1982).

[10] J. A. Wilson and A. D. Yoffe, Adv. Phys. **18**, 193 (1969).

[11] A. V. Stier, N. P. Wilson, K. A. Velizhanin, J. Kono, X. Xu, and S. A. Crooker, Phys. Rev. Lett. **120**, 057405 (2018).

[12] J. Pandey and A. Soni, Appl. Surf. Sci. **463**, 52 (2019).

[13] J. Ribeiro-Soares, R. M. Almeida, E. B. Barros, P. T. Araujo, M. S. Dresselhaus, L. G. Cançado, and A. Jorio, Phys. Rev. B **90**, 115438 (2014).

[14] G. Liu, B. Debnath, T. R. Pope, T. T. Salguero, R. K. Lake, and A. A. Balandin, Nat. Nanotechnol. **11**, 845 (2016).

[15] G. Liu, S. Rumyantsev, M. A. Bloodgood, T. T. Salguero, and A. A. Balandin, Nano Lett. **18**, 3630 (2018).

[16] M. Yoshida, R. Suzuki, Y. Zhang, M. Nakano, and Y. Iwasa, Sci. Adv. **1**, e1500606 (2015).

[17] G. Liu, E. X. Zhang, C. D. Liang, M. A. Bloodgood, T. T. Salguero, D. M. Fleetwood, and A. A. Balandin, IEEE Electron Device Lett. **38**, 1724 (2017).

[18] A. K. Geremew et al., Nanoscale **11**, 8380 (2019).

[19] A. G. Khitun, A. K. Geremew, and A. A. Balandin, IEEE Electron Device Lett. **39**, 1449 (2018).

[20] A. K. Geremew et al., ACS Nano **13**, 7231 (2019).

[21] K. Rossnagel, J. Phys.: Condens. Matter **23**, 213001 (2011).

[22] W. L. McMillan, Phys. Rev. B **16**, 643 (1977).

[23] M. D. Johannes and I. I. Mazin, Phys. Rev. B **77**, 165135 (2008).

[24] R. Samnakay, D. Wickramaratne, T. R. Pope, R. K. Lake, T. T. Salguero, and A. A. Balandin, Nano Lett. **15**, 2965 (2015).

[25] J. Zhu, H. Li, L. Zhong, P. Xiao, X. Xu, X. Yang, Z. Zhao, and J. Li, ACS Catal. **4**, 2917 (2014).

[26] P. Hajiyev, C. Cong, C. Qiu, and T. Yu, Sci. Rep. **3**, 2593 (2013).

[27] S. Tanda, T. Sambongi, T. Tani, and S. Tanaka, J. Phys. Soc. Jpn. **53**, 476 (1984).

[28] F. J. Di Salvo and J. E. Graebner, Solid State Commun. **23**, 825 (1977).

[29] S. Sun, L. Wei, Z. Li, G. Cao, Y. Liu, W. J. Lu, Y. P. Sun, H. Tian, H. Yang, and J. Li, Phys. Rev. B **92**, 224303 (2015).

[30] P. Goli, J. Khan, D. Wickramaratne, R. K. Lake, and A. A. Balandin, Nano Lett. **12**, 5941 (2012).

[31] P. Garoche, J. J. Veyssié, P. Manuel, and P. Molinié, Solid State Commun. **19**, 455 (1976).

[32] T. Valla, A. V. Fedorov, P. D. Johnson, P. A. Glans, C. McGuinness, K. E. Smith, E. Y. Andrei, and H. Berger, Phys. Rev. Lett. **92**, 086401 (2004).

[33] M. Hossain, Z. Zhao, W. Wen, X. Wang, J. Wu, and L. Xie, Crystals **7**, 298 (2017).

[34] K. Terashima, T. Sato, H. Komatsu, T. Takahashi, N. Maeda, and K. Hayashi, Phys. Rev. B **68**, 155108 (2003).

[35] C. Yadav and A. Rastogi, Solid State Commun. **150**, 648 (2010).

[36] R. A. Young, *The Rietveld Method* (Crystallography/Oxford University Press, Oxford, 1993).

[37] See Supplemental Material at http://link.aps.org/supplemental/10.1103/PhysRevResearch.2.033118 for Elemental mapping, magnetic hysteresis and Raman measurements.

[38] J. Rigoult, C. Guidi-Morosini, A. Tomas, and P. Molinie, Acta Crystallogr., Sect. B **38**, 1557 (1982).

[39] F. J. DiSalvo and J. V. Waszczak, Phys. Rev. B **23**, 457 (1981).

[40] S. Zhang *et al.*, Adv. Mater. **21**, 2282 (2009).

[41] W. Niu, M. Gao, X. Wang, F. Song, J. Du, X. Wang, Y. Xu, and R. Zhang, Sci. Rep. **6**, 26081 (2016).

[42] S. Barua, M. Hatnean, M. Lees, and G. Balakrishnan, Sci. Rep. **7**, 10964 (2017).

[43] M. Bayard and M. J. Sienko, J. Solid State Chem. **19**, 325 (1976).

[44] S. Acharya, S. Anwar, T. Mori, and A. Soni, J. Mater. Chem. C **6**, 6489 (2018).

[45] Y. Takaoka and K. Motizuki, J. Phys. Soc. Jpn. **49**, 1838 (1980).

[46] S. Sugai, K. Murase, S. Uchida, and S. Tanaka, J. Phys. Colloq. **42**, C6-740 (1981).

[47] J. A. Holy, K. C. Woo, M. V. Klein, and F. C. Brown, Phys. Rev. B **16**, 3628 (1977).

[48] J. E. Smith, J. C. Tsang, and M. W. Shafer, Solid State Commun. **19**, 283 (1976).

[49] N. Nagaosa and E. Hanamura, Phys. Rev. B **29**, 2060 (1984).

[50] I. Calizo, A. A. Balandin, W. Bao, F. Miao, and C. N. Lau, Nano Lett. **7**, 2645 (2007).

[51] Y. Hu, F. Zheng, X. Ren, J. Feng, and Y. Li, Phys. Rev. B **91**, 144502 (2015).